ORIGINAL PAPER

Thermal properties and hydrophilicity of antibacterial poly(phenylene sulfide) nanocomposites reinforced with zinc oxide-doped multiwall carbon nanotubes

Fei-Fan Ge[1,2] · Neng Wan[1,2] · Chi-Hui Tsou[1,2,3] · Jui-Chin Chen[4] · Chin-San Wu[5] · Manuel Reyes De Guzman[1,2,3] · Chun-Yan Zeng[1,2] · Li Zhou[1,2] · Yu-Ting Wang[1,2] · Xu Luo[1] · Yong-Qi Yu[1,2]

Abstract

A nanomaterial in the form of zinc oxide-doped multiwall carbon nanotubes (MWCNTs-ZnO) was synthesized, and new nanocomposites were prepared by blending together different amounts of poly(phenylene sulfide) (PPS) as matrix and MWCNTs–ZnO as fillers in a torque rheometer with an internal mixer. MWCNTs-ZnO enhanced the barrier performance of PPS in terms of crystallinity, path blocking, and coordination reaction. Through tensile test, scanning electron microscopy, X-ray diffraction, differential scanning calorimetry, thermogravimetric analysis, evaluation of *Escherichia coli* inhibition, and water permeability, the properties of pure PPS and PPS/MWCNTs-ZnO nanocomposites were characterized and compared. The results showed that MWCNTs-ZnO played a role in heterogeneous nucleation. When the content of MWCNTs-ZnO was 0.4 phr, the crystallization temperature, thermostability, tensile strength, elongation at break, and hydrophilicity approached maximum values, and the microscopic morphology changed from the original brittle fracture to a ductile fracture. PPS/MWCNTs-ZnO nanocomposites showed improved barrier performance due to three possible factors: (1) extending the transmission path due to the presence of nanofillers; (2) enhancing crystallization; (3) coordination between PPS and MWCNTs-ZnO. Finally, FTIR analysis showed that PPS and MWCNTs-ZnO formed coordination between them, which improved the properties of nanocomposites.

Keywords Polyphenylene sulfide · Zinc oxide-doped multiwall carbon nanotubes · Tensile properties · Crystallinity · Antibacterial evaluation · Water permeability · Coordination · Hydrophilicity

Highlights
- A new nanomaterial (MWCNTs-ZnO) is incorporated into PPS.
- MWCNTs-ZnO improves both tensile strength and elongation at break of PPS.
- MWCNTs-ZnO enhances the thermostability and crystallinity of PPS.
- PPS interacts with MWCNTs-ZnO through coordination.
- MWCNTs-ZnO boosts the barrier performance of PPS/ MWCNTs-ZnO nanocomposites.

Fei-Fan Ge, Neng Wan and Chi-Hui Tsou are contributed equally to this work.

✉ Chi-Hui Tsou
mayko0301@hotmail.com; tsou@suse.edu.cn

✉ Yong-Qi Yu
1206058630@qq.com

Extended author information available on the last page of the article

Introduction

Carbon nanotubes (CNTs) originated from the contributions of Smally and his collaborators to fullerene chemistry [1]. Since then, research on the synthesis of CNTs has started. CNTs are hollow structures of graphene coiled around concentric axis. They can be divided into single-wall carbon nanotubes and multiwall carbon nanotubes (MWCNTs), depending on the number of coiled layers. In recent years, CNTs have achieved excellent overall properties such as thermal, mechanical, optical, and electrical properties [2]. They are widely used as a reinforcing modifier in polymer nanocomposites. Aboutalebi et al. [3] prepared a new nanocomposite graphene oxide/MWCNTs supercapacitor. Its capacitance increased by 120%; thus, it was expected to be used in energy storage equipment. Lu et al. [4] explored the mechanical and frictional properties of nanocomposites containing different proportions of MWCNTs and

polyoxybenzoic acid, which were prepared through solution mixing, and they effectively improved the mechanical strength and frictional resistance of concrete. There are numerous studies on carbon nano-fillers, as well as on inorganic nano-fillers such as nano-zinc oxide (ZnO). Nano-ZnO is a white solid powder with low toxicity (i.e., friendly to the environment), and it has good thermal stability [5]. Because of the different polarity planes of zinc and oxygen atoms in the nano-ZnO molecular structure, nano-ZnO has strong self-polarization. Due to its excellent antibacterial properties, photocatalytic effect, and special mechanical properties, nano-ZnO has been widely used in optics, electronics, medicine, and other fields. In a study on nano-ZnO, Zhang et al. [6] deposited ZnO on graphene by means of ultrasonic spray pyrolysis. The prepared graphene-ZnO film had stronger capacitive behavior, better reversible charge and discharge capability, and higher capacitance. Zhou et al. [7] initially added ZnO to a monomer, and then polymerized them in an ultraviolet environment, so that ZnO was evenly dispersed in the polymer. The prepared polymer films had good thermal stability and improved transparency.

Poly(phenylene sulfide) (PPS) is one of the six special engineering plastics with excellent overall performance. PPS has excellent high temperature resistance, corrosion resistance, excellent insulation performance, balanced physical and mechanical properties, and excellent dimensional stability. However, it has poor toughness and brittleness, so it is modified with fillers to make various functional films and coatings, high-performance fibers, and textiles. PPS is often widely used as matrix in nanocomposite materials. Liang [8] prepared a glass fiber-reinforced PPS nanocomposite filled with nano-$CaCO_3$ in a twin-screw extruder. The results showed that nano-$CaCO_3$ had a significant reinforcing and toughening effect on PPS. Kuang et al. [9] prepared in solution a stable nanocomposite of hyperbranched PPS with silver nanoparticles, and found that it had excellent inhibitory effect on the growth of a common bacteria (*E. coli*). Najim and Ola [10] prepared samples of TiO_2 nanocomposites with different proportions of the components through melt-mixing in a double-screw extruder. The relationship between the tribological and mechanical properties of PPS nanocomposites was discussed. It was found that nanoparticles further improved the tribological properties, and the mechanical properties, impact strength, and hardness were also improved. Wang et al. [11] modified PPS with nano-SiO_2 and added various additives. It was found that the uniform dispersion of nano-SiO_2 in PPS reduced the water absorption and temperature expansion coefficient, improved the mechanical and thermal properties, and increased the service life of PPS. As such, it met the strict requirements of electronic packaging materials. Yang et al. [12] prepared MWCNTs-PPS nanocomposites by simple melt-mixing, and at the same time, Raman spectra showed that the electrical

and mechanical properties were greatly improved due to the π-π stacking between PPS and MWCNTs and the strong interaction between the filler and the matrix. Zhang et al. [13] used blending method to prepare conductive PPS/fullerene nanocomposites, which not only increased the mechanical strength of PPS, but also gave PPS good conductivity.

MWCNTs and nano-ZnO exhibit excellent characteristics, so they can be combined to prepare MWCNTs-ZnO. Sui et al. synthesized MWCNTs-ZnO and reported that it was an excellent antibacterial nanomaterial [14]. However, MWCNTs-ZnO could have other functions such as a good polymer additive. Hence, in this study, MWCNTs-ZnO was synthesized and used as an additive to prepare PPS/MWCNTs-ZnO nanocomposites with different proportions of MWCNTs-ZnO by melt-blending. Thermal crystallization, decomposition, mechanical tensile, fractured section morphology, antibacterial evaluation, and other tests were carried out. Through comprehensive analysis of various tests, we expected to achieve a PPS nanocomposite material with excellent overall performance (Table 1).

Experimental

Materials and equipment

Synthesis of MWCNTs-ZnO

ZnO (see Fig. S1) was coated on the surface of MWCNTs through a wetting dispersion method. The ratio of MWCNTs to ZnO was 6:4. MWCNTs was added to an ethanol solution, and it was dispersed using an ultrasonic bath (FS-1088 N Ultrasonic processor, SXSONIC Co. Ltd., Shanghai, China) for 3 h. Subsequently, ZnO was mixed with the MWCNTs-ethanol solution in the ultrasonic bath, and the mixture was held there for 3 h to avoid aggregation. The solution was filtered to separate ethanol; subsequently, the mixture was placed in an oven at 50 °C for 2 h to evaporate the residual ethanol; then, the oven temperature was adjusted to 150 °C to administer thermal treatment for 1 h. Finally, MWCNTs-ZnO was obtained. Figure 1 shows the synthesis of MWCNTs-ZnO.

The SEM morphology of MWCNTs-ZnO is depicted in Fig. S2a, which shows that MWCNTs was coated by nano-ZnO with a flaky structure. Hence, the morphology of MWCNTs in MWCNTs-ZnO is not evident. To delineate clearly the morphology of MWCNTs-ZnO, TEM images of MWCNTs-ZnO (Fig. S2b) were also provided. Because ZnO flakes, with a diameter of 100–300 nm, were shown to coat MWCNTs, as observed from the TEM image (Fig. S2b), ultrasonic vibration was applied to a solution of MWCNTs-ZnO, so as to expose a small amount of MWCNTs on the

Table 1 Instruments and materials

Instrument and chemicals	Description/Model	Manufacturer	Details
PPS	PPS- B8	Sichuan Zhongke Xingye Material Co. Ltd	Melting point = 283° C; Density = 1.36 g/mL at 25 °C; Appearance = granular; Tensile strength = 62.6 ± 3.2 MPa
MWCNTs	Purified MWCNTs	Zehan Co. Ltd	Length = 6.5 ± 5.5 μm; Outer diameter = 20 ± 5 nm
Nano-ZnO	ZS-20 nm	Zhixiangyi Technology Co. Ltd	Thickness = 20 nm; Diameter = 100–350 nm
Torque rheometer	567–002	Thermo Fisher Technology Co. Ltd	/
Manual vulcanizer	QYL3	Shanghai Dingye Machinery Manufacturing Co. Ltd	/
Portable autoclave sterilizer	DSX-30L	Shanghai Shen'an Medical Instrument Factory	/
Constant-temperature biochemical incubator (150 L)	LRH-150	Shanghai Yiheng Scientific Instrument Co. Ltd	/
Constant-temperature shaking incubator	BS-1E	Changzhou Jintan Liangyou Instrument Co. Ltd	/
Microcomputer-controlled electronic universal testing machine	FBS10KNW	Xiamen Forbes Testing Co. Ltd	/
Single-sided vertical laminar flow clean worktable	SW-CJ-1FD	Suzhou Antai Air Technology Co. Ltd	/
Differential scanning calorimetry	Q2000 TA	Delaware, USA	/
Scanning electron microscopy	FESEM, MIRA3 FEG-SEM	Tescan	/
TGA	HTG-1	Beijing Hengjiu Experimental Equipment Co. Ltd	/
X-ray diffraction	D2-PHASER	Bruker, Germany	/
Contact angle tester	JC2000D	Shanghai Zhongchen Digital Technology Equipment Co. Ltd	/

surface. This enabled to capture the TEM image of MWC-NTs from a MWCNTs-ZnO sample.

Figure S3 illustrates EDX data for MWCNTs-ZnO, and Table S1 lists the elemental composition of MWCNTs-ZnO. Table S1 indicates the presence of a lot of C element in MWCNTs-ZnO, and that the weight ratio of MWCNTs to ZnO is about 1.5:1.

Figure 2 shows the XRD image of MWCNTs and MWCNTs-ZnO. Typical characteristic diffraction peaks of MWCNTs were indicated at $2\theta = 25.96$ and $43.25°$. MWCNTs-ZnO had many characteristic peaks. Nano-ZnO also had many characteristic peaks.[15]. Table 2 provides data on the peaks of MWCNTs-ZnO. The average particle size was calculated using Scherrer equation. The average particle size of MWCNTs-ZnO powder was 35.36 nm, which is far less than 100 nm, which means it is nano-powder.

Sample preparation

MWCNTs-ZnO and PPS were dried in an oven at 40 and 130 °C for 4 h, respectively. PPS/MWCNTs-ZnO nanocomposites were prepared by blending different proportions of MWCNTs-ZnO and PPS in an internal mixer chamber. The mixing conditions were as follows— mixing: low speed, 80 rmp, 3 min; high speed, 200 rmp, 3 min; chamber temperature: 295 °C; MWCNTs-ZnO content: 0.1–0.5 phr; feeding order: PPS matrix was initially added, then the torque-time curve was observed, and when the curve jitter was little and became stable, MWCNTs-ZnO powder was quickly introduced to reduce the loss of the mixing rotor and to ensure uniform mixing. Figure 1 shows the process of preparing PPS/MWCNTs-ZnO nanocomposites.

Performance test

1. Tensile property test (mechanical property)

PPS/MWCNTs-ZnO nanocomposite materials were thermally pressed into a film by using a vulcanizing machine, and samples were prepared according to ASTM D-882 standard. PPS/MWCNTs-ZnO samples with different proportions of MWCNTs-ZnO and PPS were prepared and heat-treated at 130 °C for 4 h. Tensile experiment tests were carried out
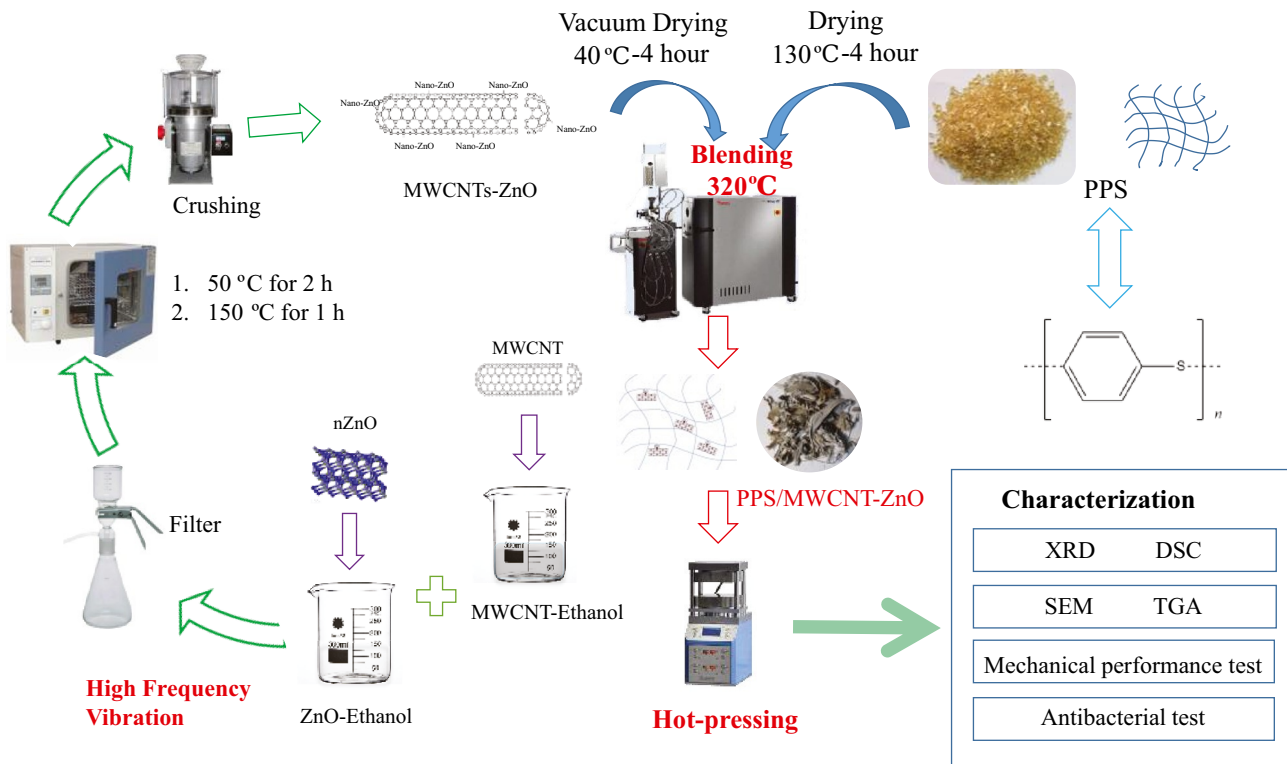
Fig. 1 Synthesis of MWCNTs-ZnO and preparation of PPS/MWCNTs-ZnO nanocomposites

using a microcomputer-controlled electronic universal testing machine; the tensile speed was 20 mm/min.

The calculation of stress was as follows:

$$\sigma = \frac{F}{A} \qquad (1)$$

where σ was the stress (N/mm^2), F the force (N), and A the cross-sectional area (mm^2).

The calculation of strain was as follows:

$$\varepsilon = \frac{\Delta l}{L} \qquad (2)$$

where ε was the strain, Δl the deformation (m), and L the sample original length (m).

2.   Differential scanning calorimetry

Samples were characterized using differential scanning calorimetry (DSC). Starting from room temperature, a 5-mg sample was heated at a rate of 10 °C/min until it reached 320 °C. This temperature was maintained constant for 3 min, and then the temperature was quickly reduced. The temperature was raised for the second time at a rate of 10 °C/min (as it was in the first heating). Then, the temperature was lowered to room temperature at a rate of 10 °C/min, and heating and cooling data were recorded.

3.   Scanning electron microscopy

The morphology of tensile fractured section was observed under various magnifications by using scanning electron microscopy (SEM, Czech VEGA 3 SBU). The test conditions were as follows: the surface was gold-plated prior to observing the cross section; images of different areas were observed at multiple magnifications of 1, 2, and 5 kx; and the energy spectrum of Zn on the material surface was obtained at 500 × and 20 kv.

4.   Thermogravimetric analysis

Samples were subjected to thermogravimetric analysis (TGA). A 10-mg heat-treated sample was weighed, and its temperature was raised to 200 °C at 10 °C/min, which was held constant for 10 min, and then the temperature was raised to 800 °C at 10 °C/min.

5.   X-ray diffraction analysis

The powder diffraction curve of nano-ZnO was measured using X-ray diffraction (XRD, German Bruker D2 PHASER). The size of the nano-filler was calculated using Scherrer equation, and the phase structure of the nano-ZnO-PPS nanocomposite was determined at the same time. The

Fig. 2 XRD patterns of (**a**) MWCNTs; (**b**)MWCNTs-ZnO
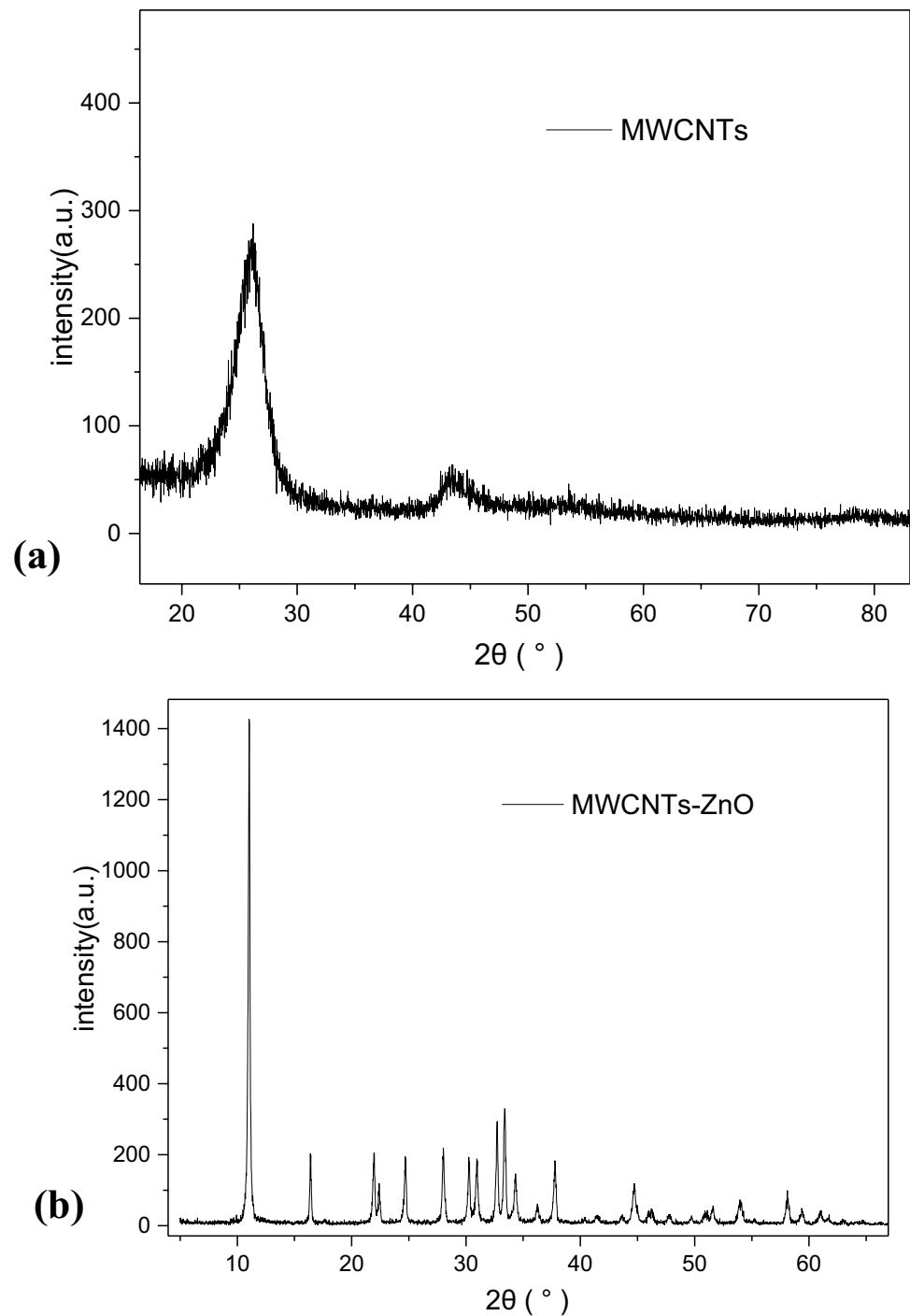
XRD data of heat-treated and unheated samples were compared. Test conditions were conducted at 5°–60° and a diffraction chamber interval of 0.1 s. Scherrer equation for calculating the size of nanomaterials is given as follows:

$$D = \frac{K\gamma}{B\cos\theta} \tag{3}$$

K is Scherrer constant, D the average thickness of the crystal grain perpendicular to the crystal plane, B the half-height or integral width of the diffraction peak of the measured sample, θ the Bragg angle, and γ the X-ray wavelength (1.54056 Å).

6. Analysis of *Escherichia coli* inhibition

Samples of heat-treated nanocomposite films with the same thickness (surface area) and mass were prepared for later use. The samples amounted to a total of 6 pieces

Table 2 XRD data for pure MWCNTs-ZnO

2θ(°)	FWHM (half-peak width)(°)	2θ(°)	FWHM (half-peak width)(°)
11.03	0.191	34.33	0.278
16.397	0.157	36.248	0.249
21.942	0.219	37.775	0.239
22.4	0.169	44.711	0.317
24.689	0.212	46.245	0.346
28.02	0.215	51.571	0.208
30.25	0.203	53.991	0.371
30.949	0.245	58.119	0.23
32.716	0.213	59.398	0.308
33.385	0.209	61.026	0.421

(including pure PPS). Agar was removed and nutrient materials were added, depending on the nutrient proportion of the culture medium. The liquid culture medium was prepared, and the solution was divided into six Erlenmeyer flasks, marked with 0, 0.1, 0.2, …, and 0.5 phr. The flasks were wrapped, sterilized, and cooled in ultra-clean platform, then inoculated against the same micro-amount of bacterial solution and shaken. The samples were placed in each of the six labeled Erlenmeyer flasks, wrapped, and shaken for 12 h in the shaking incubator.

The analysis involved the preparation of a culture medium, mixing of materials following a procedure, pH adjustment, heating and dissolution, sterilization, and use of super clean table for cooling and standby. The dilution of a sample, such as pure PPS culture medium or PPS/MWCNTs-ZnO-0.1phr culture medium, was as follows. Eight long cylindrical test tubes were prepared, each marked as 10, 10^2, …, and 10^8, into which 9 mL sterile water was added. Pure PPS culture medium contained in an Erlenmeyer flask was diluted ten-fold, then a sterile pipette was used to remove 1 mL of the pure PPS culture medium broth, and it was added to the test tube labeled "10"; afterward, the tube was shaken in an even fashion. The pipette tube was replaced, and 1 mL of liquid was drawn or taken from the 10-mark test tube. The diluent was added to the 10^2-labeled test tube, which was then shaken evenly. The operation was repeated until the 10^8-labeled test tube was 10^8-fold diluted. During the seventh and eighth dilutions, 0.1 mL liquid was taken from the middle part of the petri dish, then the culture medium was poured into a petri dish in batches and cooled to about 45° C, with slight horizontal shaking of the dish, so that the culture medium was mixed fully and the bacterial solution solidified horizontally. After 24 h of incubation in the incubator, counting of surviving colonies was done (3 groups of dilution were selected, and the average value was taken). The operation was repeated in counting the number of surviving colonies for the other nanocomposite materials.

At the same time, it should be noted that the number of colonies selected should be less than 30, between 30 and 300, or greater than 300, and the dilution ratio should be reduced or expanded.

7. Water permeability

A Languang W3/060 water vapor transmission rate test system was used to evaluate the water vapor permeability, which was measured through a vapor-permeable cup weighing method.

The nanocomposite material was passed through a vulcanizer, where it was hot-pressed, then quickly cooled to form a film. A standard circular cutter was used to prepare film samples in the form of standard water-permeable circular samples (4 samples for each nanocomposite containing the same proportion of components) for the water vapor transmission rate test. Two of the samples were heat-treated in an oven at 230 °C for 4 h to prepare heat-treated water-permeable test samples, which were fixed on a moisture-permeable cup for testing. The test parameters were as follows: humidity of instrument chamber: 90%; test temperature: 38 °C; test interval: 4 h/time (4 times for each sample, one cycle every 16 h). And the moisture permeability coefficient for the film was recorded.

8. Water contact angle

A certain area of a rectangular mechanical film was cut, and it was tested on a contact angle measuring instrument at 26 °C. To eliminate the influence of gravity on the contact angle, a micro syringe was used to measure and control the volume of the water droplet at about 2 μL. The contact angle for a drop of water contacting the sample was measured after 15 s. Each sample was subjected to 4–5 repeated contact angle determinations, and the average value was taken.

The larger the contact angle, the lower the wettability of liquid to solid. An enlarged view of the contact angle of a certain sample is shown in Fig. S4. The contact angle is calculated through a five-point fitting method, by using the following contact angle equilibrium mechanics equation:

$$R_{sy} = R_{sl} + R_{ly}\cos\theta$$

where R_{sv}, R_{sl}, and R_{lv} are the equilibrium forces experienced by water molecules at the point of intersection of solid, liquid, and gas. After simplification, the vertical downward gravity and vertical upward supporting force of water molecules are drawn. R_{sv} represents the outward traction force of water molecules from the surface free energy of solid and gas; R_{sl} refers to the internal traction force of liquid from the surface free energy of solid and liquid; R_{lv} stands

for the tangential traction force of droplets from the surface free energy of liquid and gas; θ is the contact angle. When the solid, liquid, and gas phases are determined, the contact angle is the fixed value.

Results and discussion

Tensile properties

Figure 3 shows the tensile strength and elongation at break of PPS/MWCNTs-ZnO nanocomposites with different amounts of MWCNTs-ZnO. It can be seen that when MWCNTs-ZnO nano-filler was added, the tensile strength and rupture of the nanocomposites increased with the MWCNTs-ZnO content. When the MWCNTs-ZnO content increased to 0.4 phr, the elongation and strength of the sample reached a maximum value of 7.9% and 77.5 MPa, respectively. As the MWCNTs-ZnO content increased to 0.5 phr, there was a tendency for MWCNTs-ZnO to agglomerate [16], and this led to a decrease in the mechanical properties of the nanocomposites.

Scanning electron microscopy images

Figure 4 illustrates the morphology of the tensile fractured surface of pure PPS and PPS/MWCNTs-ZnO nanocomposites with different amounts of MWCNTs-ZnO. Figure 5 depicts the surface scanning energy spectra of various PPS/MWCNTs-ZnO nanocomposites. When the MWCNTs-ZnO content was 0.1–0.4 phr, the fillers could be evenly dispersed in the PPS matrix. The fractured surface of

pure PPS showed a brittle fracture, and a large number of residual fragments on the fractured section was visible. When 0.1 phr MWCNTs-ZnO was added, the residual mass on the cross-section of the nanocomposite material was reduced. As shown in Fig. 4b, the brittle fractured phase of the material was greatly lessened. With increase in the content of fillers, the brittle fracture gradually decreased or even disappeared, and the fractured surface gradually became smooth. When the concentration of fillers was 0.4 phr, the fractured surface was completely transformed into a more ductile fracture, and some crazing fracture creases appeared [17]. At this point, the fracture morphology was uniform, and at this condition, macroscopic mechanical properties were maximum [18]. Figure 5 shows the distribution of Zn element in the nanocomposites. The dispersion of nano-fillers in the PPS substrate can be directly proved from the distribution of the Zn element. As expected, zinc was not present in pure PPS (see Fig. 5a). From Fig. 5b–e, it can be observed that MWCNTs-ZnO was evenly dispersed and well distributed. Figure 5f shows that the nano-filler has partial agglomeration. From the comparison between Figs. 4f and 5f (MWCNTs-ZnO content was 0.5 phr), the fracture surface was fragmentary, and large areas with depressed parts appeared, due to the high filler content in the nanocomposite. Excessive fillers resulted in agglomeration. As shown in Fig. 5f, many MWCNTs-ZnO particles are indicated by enclosing them with white circles, while the other parts show a small number of particles, and the remaining parts have no particles. Therefore, it can be concluded that stress was not concentrated, and mechanical properties were decreased.

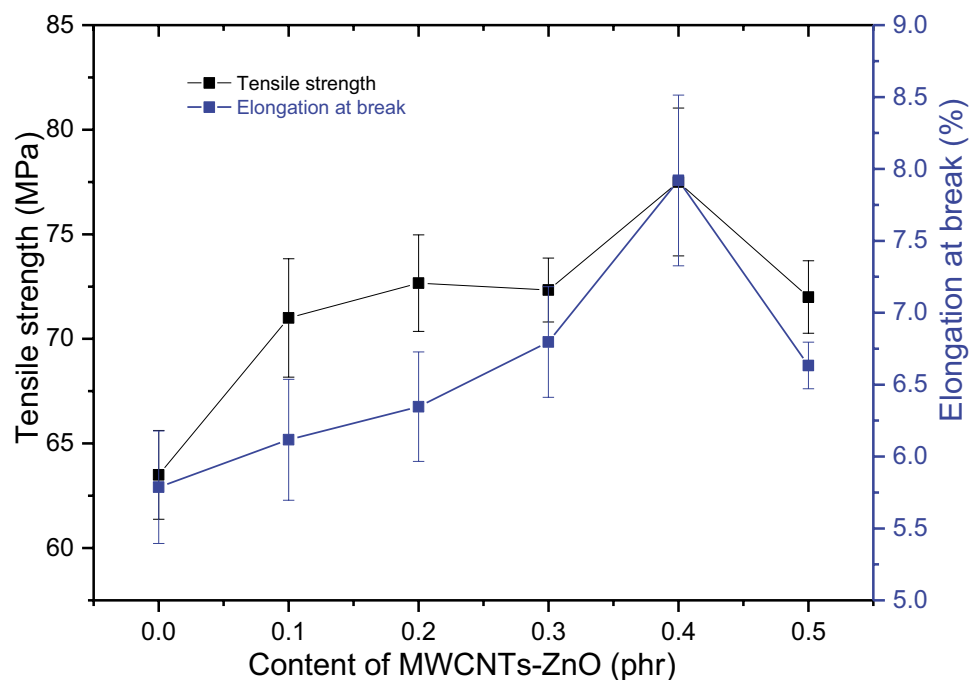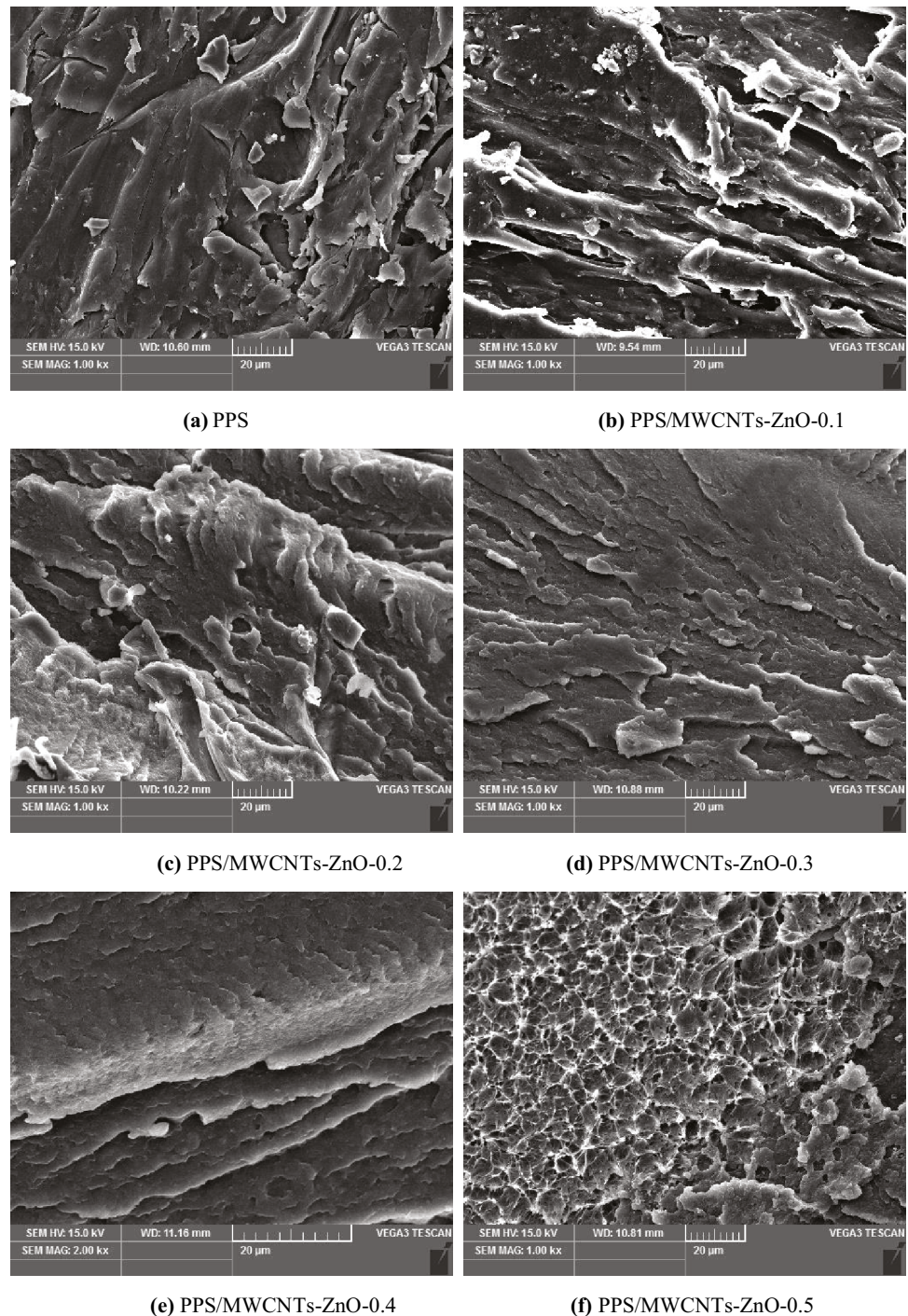**Fig. 3** Tensile strength and elongation at break of various PPS/MWCNTs-ZnO nanocomposites

Fig. 4 SEM images of various PPS/MWCNTs-ZnO nanocomposites

(a) PPS

(b) PPS/MWCNTs-ZnO-0.1

(c) PPS/MWCNTs-ZnO-0.2

(d) PPS/MWCNTs-ZnO-0.3

(e) PPS/MWCNTs-ZnO-0.4
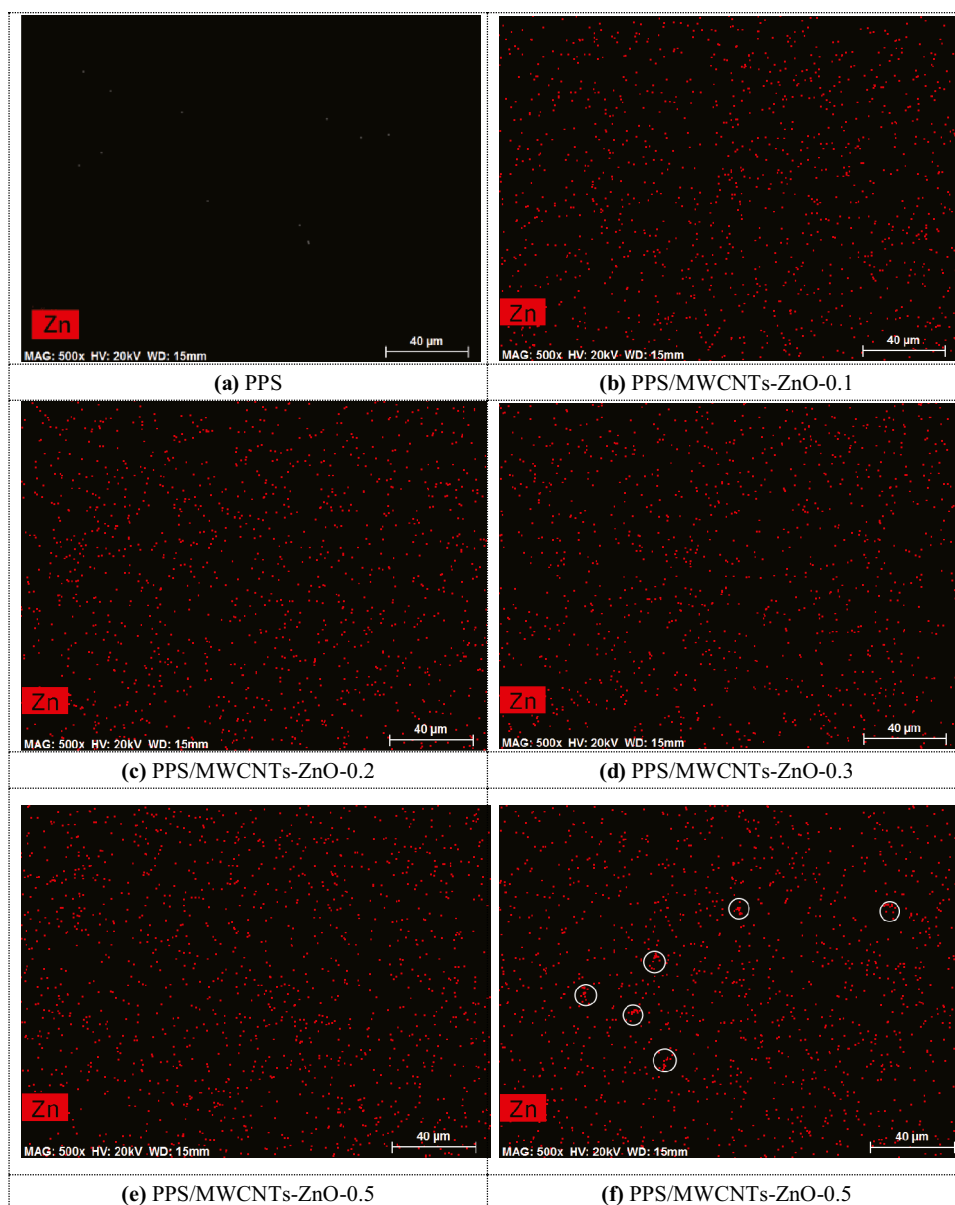
(f) PPS/MWCNTs-ZnO-0.5

X-ray diffraction spectra

Figure 6 shows the XRD diffraction patterns (crystallinity data) of PPS and PPS/MWCNTs-ZnO nanocomposites. In Fig. 1, it can be observed that the MWCNTs-ZnO sample had a strong diffraction peak at about $2\theta = 11°$, which is a typical ZnO peak. But for the nanocomposites, there is no diffraction peak at 11° because of the low content of fillers. Peaks at $2\theta = 18.63$ and 20.35 refer to the characteristic peaks of PPS. When the MWCNTs-ZnO was increased, the peaks did not shift, indicating no change in the lattice type of the PPS crystal. MWCNTs-ZnO particles occupied a certain position in the PPS crystal lattice [19], which had a heterogeneous effect on PPS and accelerated the crystallization. More positions in the PPS crystal lattice would be occupied with the addition of more MWCNTs-ZnO, resulting in further acceleration of the crystallization rate and increase in crystallinity of PPS. When the concentration

Fig. 5 EDS of various PPS/
MWCNTs-ZnO nanocomposites

(a) PPS

(b) PPS/MWCNTs-ZnO-0.1

(c) PPS/MWCNTs-ZnO-0.2

(d) PPS/MWCNTs-ZnO-0.3

**(e)** PPS/MWCNTs-ZnO-0.5

(f) PPS/MWCNTs-ZnO-0.5

of fillers reached 0.4 phr, the nanocomposite crystallinity reached its maximum, and the uniformly dispersed filler in the PPS matrix reached saturation [20]. Although the addition of more MWCNTs-ZnO accelerated the crystallization of PPS, filler agglomeration appeared within the crystal gaps due to the high content of MWCNTs-ZnO. Even the PPS crystallization sites were occupied by several MWCNTs-ZnO; as such, complete crystallization was not attained, so the overall crystallinity was decreased.

DSC curve analysis

Figure 7 provides the following data: recrystallization from second heating curves (Fig. 7a), melting temperature from second heating curves (Fig. 7b), crystallization from cooling curves (Fig. 7c), and glass transition temperature (T_g) from second heating curves (Fig. 7d). Figure 7b, d and Table 3 show that melting and glass transition temperatures basically had little change. As the content of MWCNTs-ZnO increased, T_c shifted significantly to the right, and it was higher than that of pure PPS. When the content of MWCNTs-ZnO increased to 0.4 phr, T_c shifted to the right, and T_c significantly increased by 11 °C. Further increasing the content of MWCNTs-ZnO to 0.5 phr decreased T_c. The results also showed that MWCNTs-ZnO could play a role in nucleation and could increase the crystallization rate. When the content of MWCNTs-ZnO was too high, fillers would agglomerate, which cause slight reduction in the crystallization rate. At the same time, the recrystallization temperature (T_{c1}) was the lowest when the content of MWCNTs-ZnO reached 0.4

Fig. 6 X-ray diffraction patterns of PPS and various PPS/MWC-NTs-ZnO nanocomposite films
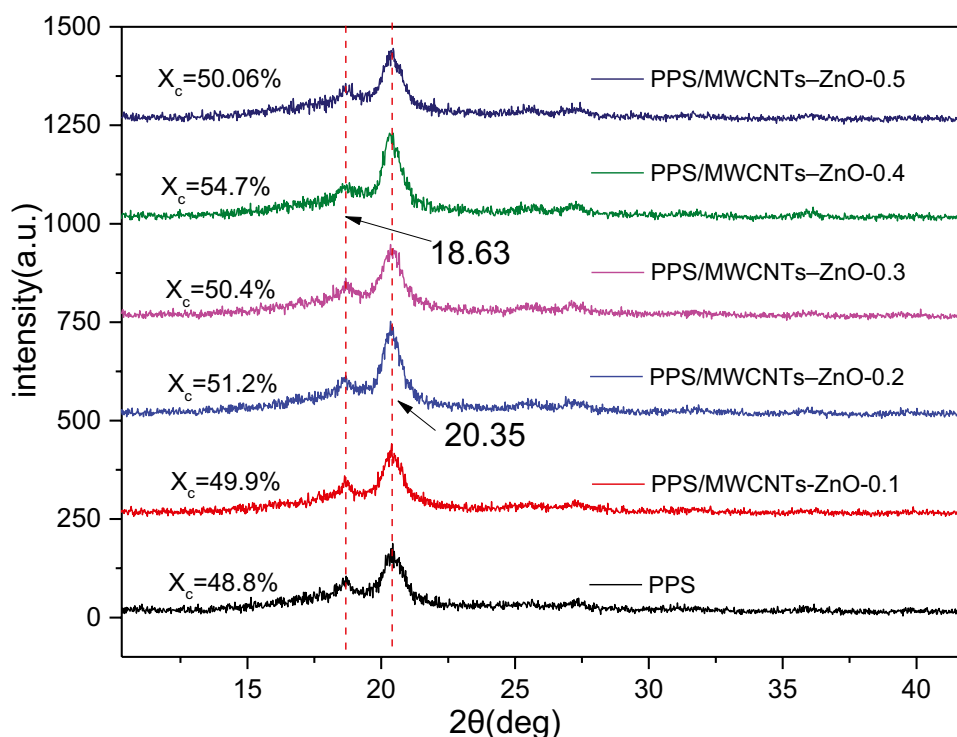
phr, providing evidence that the crystallization rate of PPS could reach the highest at 0.4 phr MWCNTs-ZnO [21–23].

The calculation formula for X_c is as follows:

$$X_c^w = \frac{\Delta H_m}{\Delta H_C} \tag{4}$$

$$X_c = (1 + \frac{Pr}{100})X_c^w \tag{5}$$

where X_c^w: melting crystallinity; ΔH_m: melting enthalpy; ΔH_c: melting enthalpy of 100% crystalline PPS ($= -80.94$ J/g) [24]; X_c: modified crystallinity of PPS nanocomposite.

From Table 3, the crystallinity of nanocomposites increased with the filler content (the addition of MWC-NTs-ZnO was up to 0.4 phr). Then, the crystallinity clearly decreased when the filler content was 0.5 phr. The trend in the change of crystallinity is similar to that in the previous discussion of XRD.

Data from thermogravimetric analysis

A data chart for water loss as a function of temperature in the range 200–800 °C is given in Fig. 8, which shows TGA (under nitrogen atmosphere) for PPS/MWCNT-ZnO nanocomposites with different proportions (0–0.5 phr) of MWCNT-ZnO and PPS. Tables 3 and 4 list the temperature corresponding to the highest decomposition rate for PPS/MWCNT-ZnO nanocomposites. When the temperature reached 600 °C, the weight loss of pure PPS exceeded 80%. Increasing the filler content not only could slow down the thermal degradation of PPS nanocomposites, but also could reduce the weight loss at high temperatures. According to the TGA diagram, the decomposition of pure PPS was equal to 510.69 °C at Td_{max} (the temperature at the maximum decomposition rate). T_{dmax} of the PPS nanocomposite material increased with the modifier content. When the content of MWCNTs-ZnO increased to 0.4 phr, T_{dmax} of the nanocomposite material reached the maximum value of 552.39 °C. When MWCNTs-ZnO was further added, T_{dmax} of the PPS nanocomposite was still 39.88 °C higher than that of pure PPS, although it decreased compared with T_{dmax} in the case of the nanocomposite with 0.4 phr modifier. That is to say, the addition of MWCNTs-ZnO increased not only the thermal stability of PPS, but also the residual weight loss of the nanocomposite (see Table 4). This may be because MWCNTs-ZnO occupied the PPS lattice points, accelerated the crystallization of PPS, and reduced the intermolecular gap between the molecules [25]. At the same time, the chemical bond energy of the crystal formed by MWCNTs-ZnO and PPS was higher than that of pure PPS crystal. As the MWCNTs-ZnO content increased, more and more PPS molecular chains were linked by MWCNTS-ZnO, so more thermal energy was required to break them [26]. Kissinger method [27, 28] can be used to calculate the trend in activation energy change. The equation is as follows:
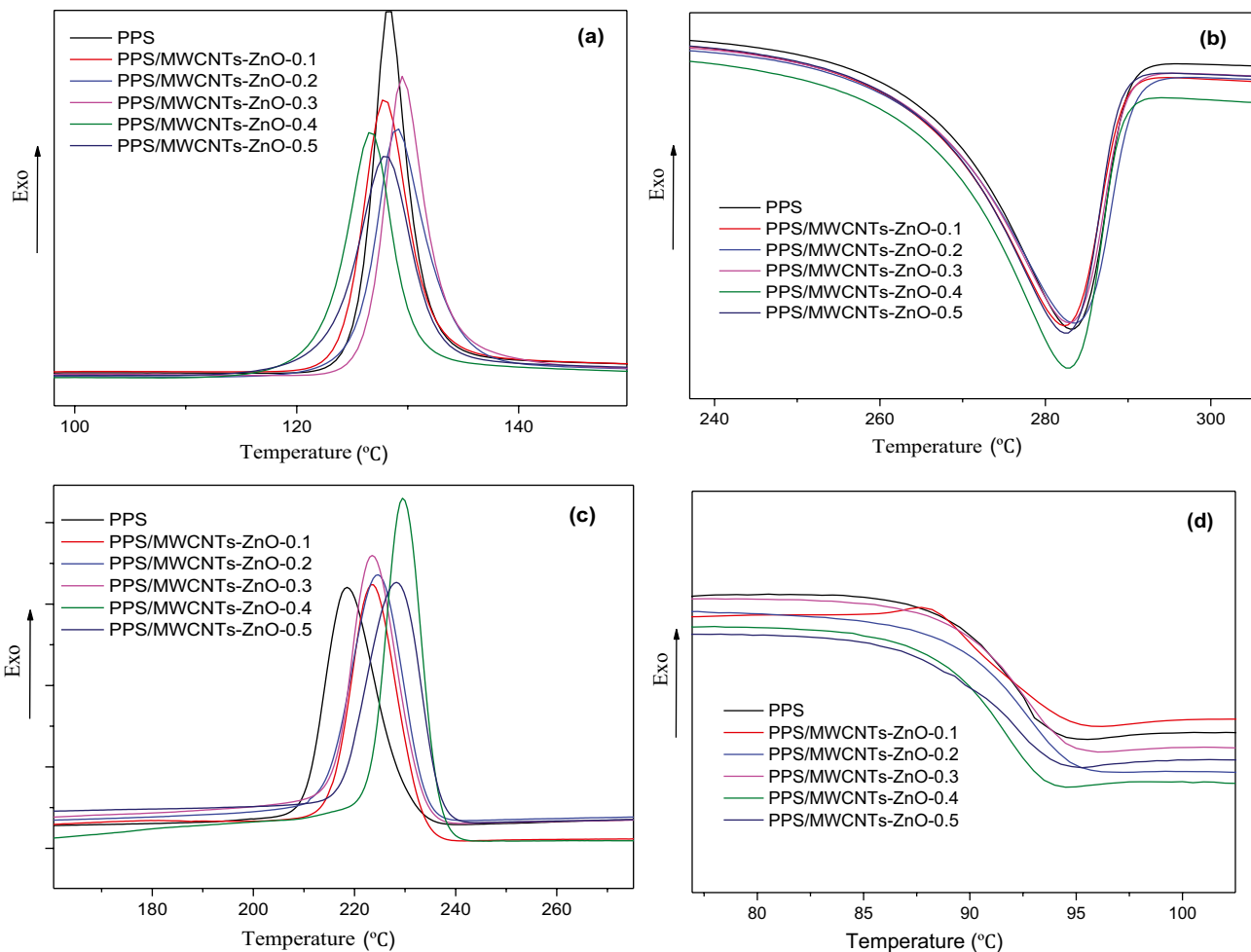
Fig. 7 Non-isothermal DSC curves for PPS and various PPS/MWC-NTs-ZnO nanocomposites: (**a**) second heating curves indicating recrystallization peaks; (**b**) second heating curves indicating melting peaks; (**c**) cooling curves indicating crystallization peaks; (**d**) second heating curves indicating glass transition temperatures

$$\ln\left(\frac{\beta}{T_{dmax}}\right) = \ln\frac{AR}{E_a} - \frac{E_a}{RT_{dmax}} \qquad (6)$$

where β is the heating rate: 10 °C/min; T_{dmax} the temperature corresponding to the maximum heating rate, °C; A the pre-exponential factor for pure PPS: 2.9×10^9 kJ/mol; R the gas constant: 8.314×10^{-3} kJ/(mol·K); E_a the reaction activation energy at the temperature corresponding to T_{dmax}.

Data on activation energy are given in Table 4. The activation energy increases with the addition of MWCNTs-ZnO (≤ 0.4 phr), and the activation energy of PPS/MWCNTs-ZnO nanocomposites at T_{dmax} also increases, indicating that the nanocomposites require more energy for decomposition and fracture. When the content of MWCNTs-ZnO $= 0.5$ phr, the activation energy at T_{dmax} became smaller, and it may be due to the agglomeration of excess MWCNTs-ZnO or

Table 3 DSC parameters for PPS and various PPS/MWCNTs-ZnO nanocomposites

PPS	T_g (°C)	T_{c1} (°C)	T_m (°C)	ΔH_m (J/g)	Xc (%)	T_c (°C)
PPS	91.0	128.3	283.1	-38.90	48.06	218.6
PPS/MWCNTs-ZnO-0.1	88.4	127.9	282.3	-38.98	48.16	223.8
PPS/MWCNTs-ZnO-0.2	89.7	129.5	282.9	-39.11	48.46	223.7
PPS/MWCNTs-ZnO-0.3	89.5	129	283.4	-40.11	49.66	224.6
PPS/MWCNTs-ZnO-0.4	88.5	126.7	282.5	-40.67	50.44	229.6
PPS/MWCNTs-ZnO-0.5	88.1	128	282.4	-39.87	49.51	228.4

Fig. 8 TGA diagrams for various PPS/MWCnTs-ZnO nanocomposites
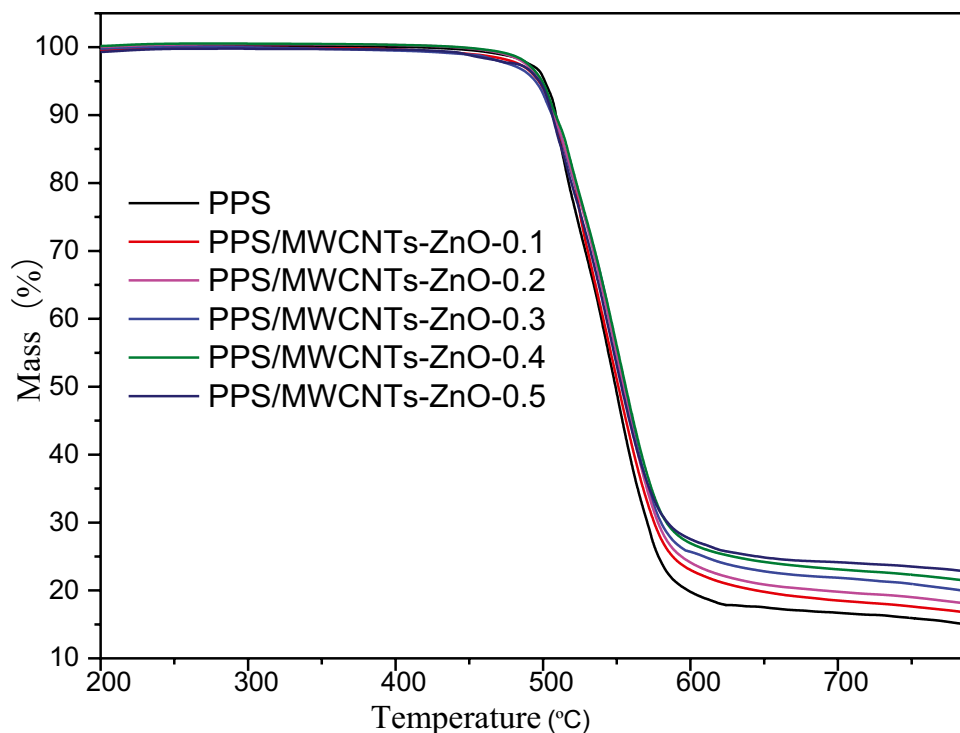
its dispersion between the PPS crystals in the nanocomposite material. But it could not be combined with the PPS crystals and distributed between them, which increased the gap between adjacent crystals and greatly reduced the Van der Waals force between the PPS crystals, resulting in the decrease of the overall bond energy, thereby decreasing the thermal stability of the nanocomposite [29].

Antimicrobial activity

Figure 9 compares the number of *E. coli* colonies in nanocomposite PPS/MWCNTs-ZnO materials with various proportions of MWCNTs-ZnO and PPS. The effect of pure PPS on *E. coli* was minimal. When 0.1 phr MWCNTs-ZnO was initially added, the nanocomposite already had excellent antibacterial properties. MWCNTs-ZnO occupied the

PPS crystal array and formed mosaic or uniform dispersion around or even inside the nanocomposite. When it came into contact with *E. coli*, MWCNTs-ZnO played a role: Zn^{2+} entered into *E. coli* and destroyed the cell structure, thereby inactivating *E. coli* and reducing it to an *E. coli* strain [30]. The number of colonies per milliliter dropped rapidly, and then as the filler amount increased, there were more and more uniform nano-fillers in the nanocomposite material. At the same time, the contact area between the nano-fillers and *E. coli* continued to enlarge, which led to a continuous defeat of *E. coli*. When the content of nano-fillers increased to 0.5 phr, the fillers were already in the saturation stage and tended to agglomerate. Too much MWCNTs–ZnO led to its complete exposure, and the contact with *E. coli* resulted in a rapid decline in the number of bacterial strains.
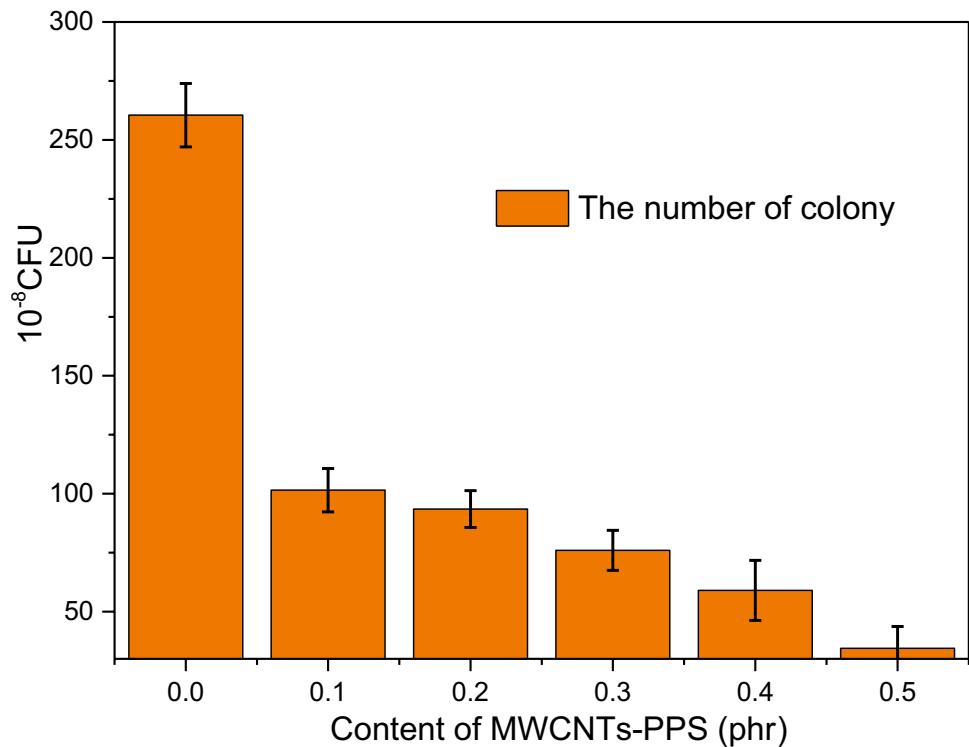
Permeability coefficient

Figure 10 presents a diagram of water permeability for PPS/MWCNTs-ZnO nanocomposites containing various proportions of MWCNTs-ZnO and PPS. The permeability coefficient of pure PPS material was 12.69×10^{-15} g.cm/cm^2.s.Pa. With the addition of MWCNTs-ZnO, the permeability coefficient of PPS nanocomposites changed. There are three possible reasons for this change. First, the initial small amount of MWCNTs-ZnO was used for heterogeneous nucleation, and it affected the crystallization of the PPS matrix. Second, the permeation path of water would be extended on account of the MWCNTs-ZnO barrier, whose effect was to

Table 4 Temperature corresponding to maximum decomposition rate for various PPS/MWCNTs-ZnO nanocomposites

| Sample	T_{dmax} (°C)	Activation energy for T_{dmax} (KJ/mol)	Residual at 800 °C (%)
PPS	510.69	146.69	9.77
PPS/MWCNTs-ZnO-0.1	525.03	149.53	11.48
PPS/MWCNTs-ZnO-0.2	544.14	153.43	12.84
PPS/MWCNTs-ZnO-0.3	551.73	154.69	14.65
PPS/MWCNTs-ZnO-0.4	552.39	154.76	16.22
PPS/MWCNTs-ZnO-0.5	550.57	154.19	17.60

Fig. 9 Number of *Escherichia coli* colonies in PPS and various PPS/MWCNTs-ZnO nanocomposites

prevent water vapor transmission. The crystallinity of PPS was expanded, the arrangement was more orderly, and the internal gap was reduced; as a result, the water molecules were unable to pass through and the permeability coefficient of the nanocomposite material was reduced [31]. The higher the MWCNTs-ZnO, the lower the permeability coefficient, and the PPS matrix crystallinity further expanded and more and more PPS matrix changed from an unsteady phase to a crystalline phase, making it more difficult for water molecules to pass through. When the MWCNTs-ZnO content

Fig. 10 Water permeability coefficient of various PP/MWCNTS-ZnO nanocomposites
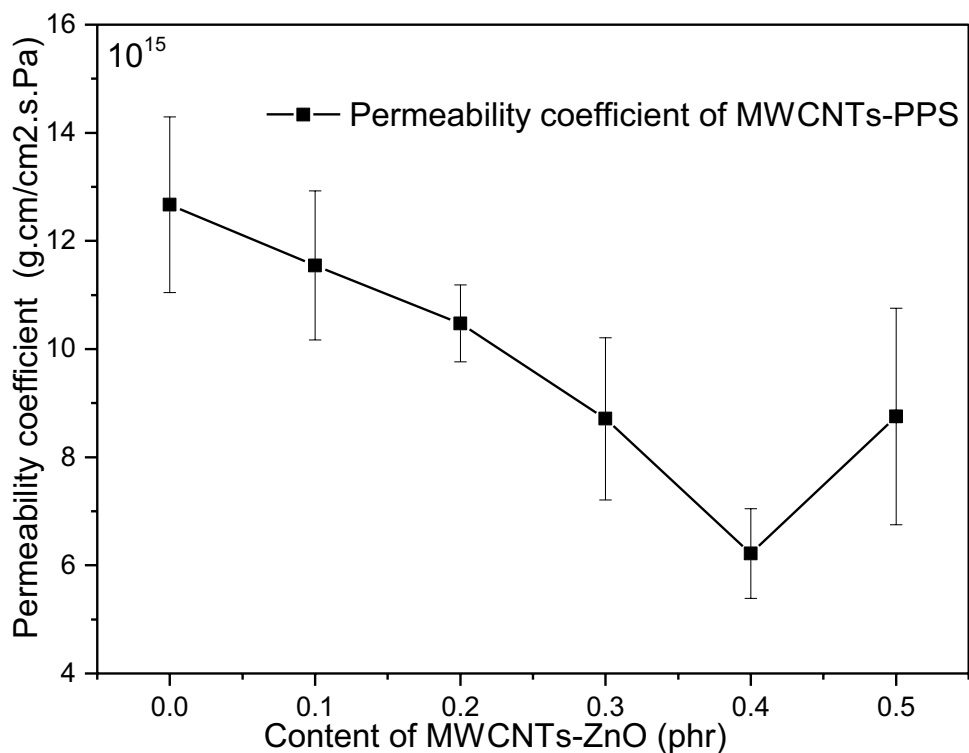
reached 0.4 phr, the permeability coefficient of water molecules reached the minimum value of 6.2018×10^{-15} g.m/cm^2.s.Pa, and the reduction ratio was more than 50% of the ratio for pure PPS. When MWCNTs-ZnO was continually added until it reached 0.5 phr, packing phenomenon occurred in the nanocomposites. This packing restricted the PPS crystallization and increased difficulty of crystallization, leading to decreased crystallization [32]. The nanocomposite may even be transformed near the crystalline phase,

at which the particles apparently clustered together, creating internal spaces in the nanocomposite material. This defect increased the chances for water molecules to go through, increasing the permeability coefficient of the PPS nanocomposite with 0.5 phr MWCNTs-ZnO.

The third reason for improving the barrier efficiency is that the change in the permeability coefficient may be due to the formation of coordination bond between the sulfur atoms in PPS and Zn^{2+} in MWCNT-ZnO [33]. The result was to make

Fig. 11 (a) Formation of coordination bonds between sulfur atoms in PPS and Zn^{2+} in MWCNT-ZnO; (b) barrier to water vapor permeation imposed by MWCNTs-ZnO added to PPS matrix
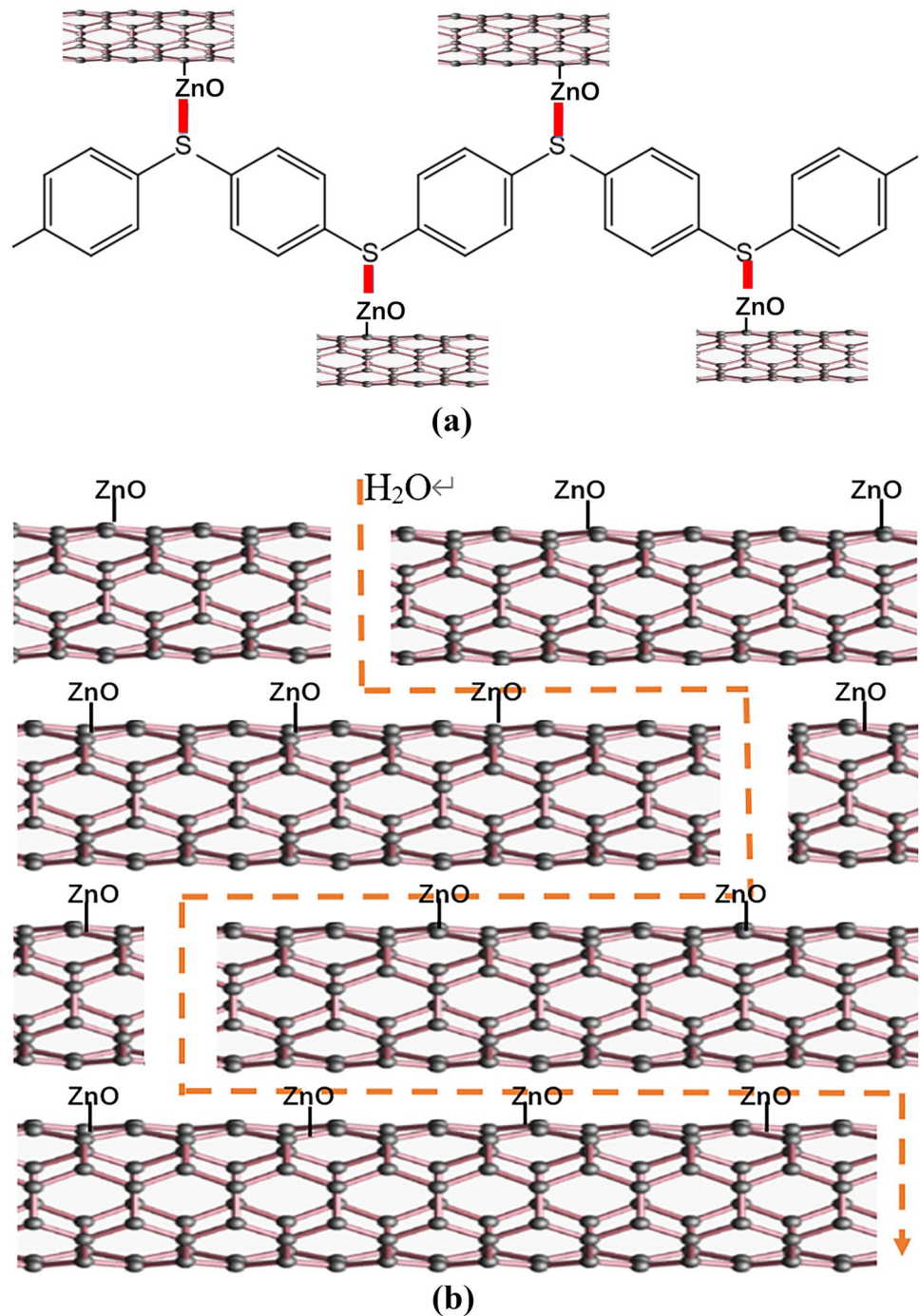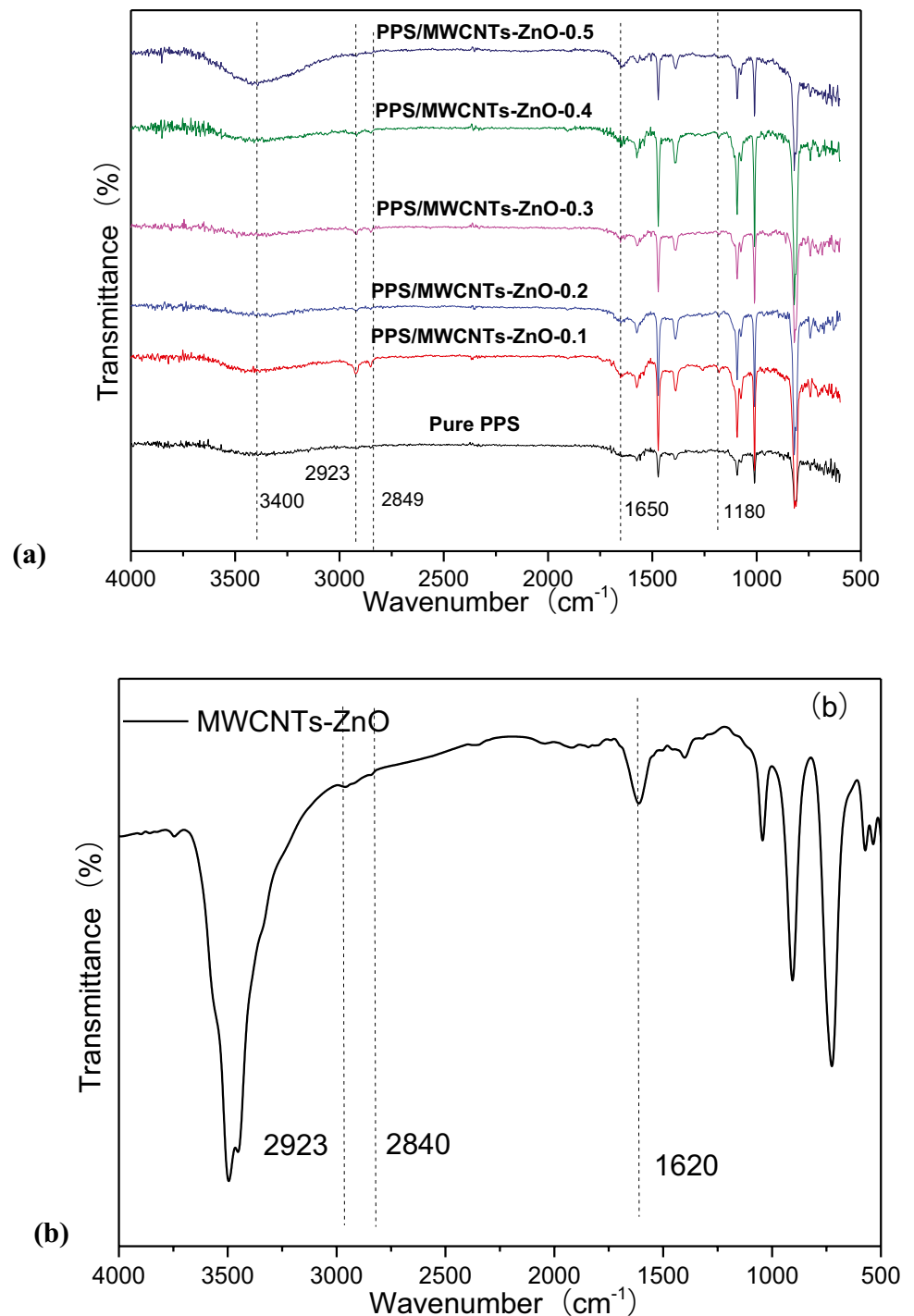
Fig. 12 FTIR diagram for MWCNTs-ZnO and various PPS/MWCNTs-ZnO nanocomposites

the PPS crystals closer to each other, as shown in Fig. 11a. The red coordination bond induced the combination of MWCNTs-ZnO and PPS to form steric hindrance effect [34]. When a small amount of MWCNTs-ZnO was added, the nanocomposite filler could be evenly dispersed between the PPS molecular chains, due to the high steric hindrance effect of MWCNTs [35–37]. As the filler amount increased, more and more gaps between the PPS molecular chains (crystalline and amorphous phases) were occupied by the filler-doped nanocomposite, so that the water molecules must take a longer path to pass through, resulting in decreased permeability coefficient, as shown in Fig. 11b. The permeation path of water molecules expanded, and the permeation efficiency decreased. When the nanocomposite filler content reached 0.5 phr, a large amount of MWCNTs-ZnO occupied the PPS crystalline lattice to form hollow points in the nanocomposite material, which in turn expanded the voids in the PPS

Fig. 13 Water contact angle of PPS and various PPS/MWC-NTS-ZnO nanocomposites
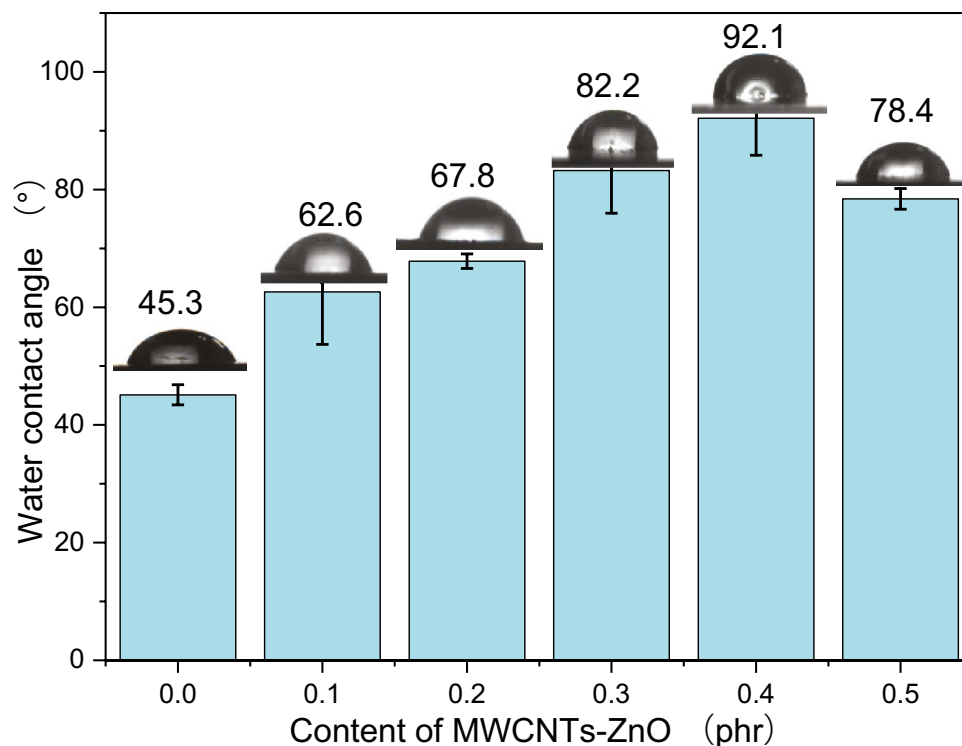
matrix, and this is conducive to the penetration of water molecules, resulting in an expansion of the permeability coefficient.

Figure 12 shows the FTIR data for PPS and various PPS/MWCNTs-ZnO nanocomposites, as well as for MWCNTs-ZnO. A wavenumber of 3440 cm^{-1} referred to the $O-H$ vibration peak, which was caused by a small amount of water molecules in the PPS molecule and the water molecules brought in by MWCNTs. Relative to pure PPS, new bands at 2923 and 2849 cm^{-1} described stretching vibration peaks and deformation vibration peaks of $-CH_3$ and $-CH_2-$ in the MWCNTs, as shown in Fig. 12b. The $C=O$ stretching vibration peak at 1620 cm^{-1} may come from $-COOH$ of MWCNTs in MWCNTs-ZnO (Fig. 12b), which could form hydrogen bonds with PPS [38], promoting the improvement of mechanical properties. In addition, the nanocomposite material had a new weak peak at 1180 cm^{-1}, which might be the symmetric stretching vibration of sulfonyl ($-SO_2-$) or thionyl ($-S=O$) [39, 40]. This may be due to the presence of vacant orbitals in the isolated MWCNTs-$Zn^{2+}O^{2-}$ and the metal Zn^{2+} exposed by MWCNT-Zn^{2+} in the nanocomposite material, forming coordination bonds with $-S-$, which caused ph–S–ph to be positively charged $(2+)$ to satisfy Hund's rule [41]. The electron pair of O^{2-} entered the S orbital to form a covalent bond, forming an $-S=O$ bond. With the increase in nanomaterials, a large number of MWCNTS-Zn^{2+} formed coordination bonds with S atoms, which increased the ph–S–ph positive state, and more and more O^{2-} entered the electron orbitals

of S atoms, resulting in the formation of $-SO_2-$. Thus, the tensile and barrier properties were greatly improved.

Water contact angle

Figure 13 is a chart showing the trend of contact angles for PPS and PPS/MWCNTs-ZnO materials. The contact angle of pure PPS was 45.3°. When MWCNTs-ZnO was added, the contact angle of the resulting nanocomposite material changed significantly. The contact angle increased as the content of MWCNTs-ZnO increased. When the content of MWCNTs-ZnO was 0.4 phr, the contact angle reached the maximum value of 92.1°. The presence of MWCNTs-ZnO exerted an effect, which was to improve the compactness of the nanocomposite structure, leading to improved crystallinity and increased hydrophobicity of PPS. When the nano-filler was 0.4 phr, the structure of the nanocomposite material was most compact, which provided further proof for the best barrier capacity [42, 43]. MWCNTs-ZnO was continuously added until its composition in the nanocomposite reached 0.5 phr. As a result, MWCNTs-ZnO began to agglomerate, and the smooth surface of the nanocomposite material was reduced and defects, such as micropores, also formed [44]. A rough surface with defects when in contact with water droplets would made it easier for the water molecules to enter the interior of the nanocomposite material. As such, the contact angle decreased [45].

Conclusion

PPS/MWCNTs-ZnO nanocomposites were prepared by simple mixing and melt blending. A content of ≤ 0.4 phr MWCNTs-ZnO could be uniformly dispersed in the PPS matrix, and this could enhance the performance of PPS. The nanocomposite material with 0.4 phr fillers had the best overall performance. A comprehensive comparison of the SEM microscopic morphology and tensile properties of each tensile section showed that the fractured section changed from the initial brittle fracture to a ductile fracture.

When the MWCNTs-ZnO content was 0.4 phr, it played a crucial role in heterogeneous nucleation in terms of accelerating the crystallization rate of PPS and increasing the crystallinity of PPS. At the same time, MWCNTs-ZnO occupied the PPS crystal lattice points (crystal array of PPS), and this led to stronger interaction between PPS chain bonds and greater bond energy. Relative to pure PPS, therefore, the nanocomposite material experienced not only increased T_{dmax} (an increase by 41.7 °C), but also higher residual thermogravimetric loss (residual weight loss) of the PPS nanocomposites.

The change in the permeability coefficient of PPS/MWCNTs-ZnO nanocomposites may be ascribed to three reasons. First reason was the expansion of crystallinity, which caused the permeability coefficient of PPS nanocomposites to decrease with the increase in nanocomposite fillers. Second was the formation of coordination bonds between a small amount of Zn^{2+} and the S atom in PPS molecular chains, making the chains more compact. For the third and final reason, a small amount of MWCNTs-ZnO was evenly dispersed in the PPS matrix. When MWCNTs were dispersed in the PPS matrix, an effective steric hindrance was formed, causing the water molecules to be more compact. The permeation of water molecules must go through a longer path, which reduced the water vapor transmission rate. Regardless of the reason, the explanation can be obtained from a macroscopic viewpoint. The water molecule barrier effect for the PPS nanocomposite was the best when the MWCNTs-ZnO content was 0.4 phr. The water permeability coefficient was the lowest, and various properties approached the highest value. This new type of nanocomposite, which had potential to be a new type of engineering nanocomposite, could deliver excellent overall performance with the addition of an optimal content of nano-fillers. Finally, FTIR analysis also proved that PPS and MWCNTs-ZnO interacted with each other through some form of coordination, which greatly enhanced the properties of the nanocomposites.

Supplementary information The online version contains supplementary material available at https://doi.org/10.1007/s10965-022-02931-9.

Declarations

Conflicts of interest The authors declare no conflicts of interest.

References

1. Zhang Q, O'Brien SC, Heath JR, Liu Y (1986) Cheminform abstract: reactivity of large carbon clusters: spheroidal carbon shells and their possible relevance to the formation and morphology of soot. Chem Infor Dienst 17(22). https://doi.org/10.1021/j100276a001

2. Kamkar M, Sultana SMN, Pawar SP, Eshraghian A, Sundararaj U (2020) The key role of processing in tuning nonlinear viscoelastic properties and microwave absorption in cnt-based polymer nanocomposites. Mater Today Commun 24:101010. https://doi.org/10.1016/j.mtcomm.2020.101010

3. Aboutalebi S, Chidembo A, Salari M, Konstantinov K, Wexler D, Aboutalebi S, Chidembo A et al (2011) Comparison of go, go/mwcnts composite and mwcnts as potential electrode materials for supercapacitors. Energy Environ Sci. https://doi.org/10.1039/C1EE01039E

4. Lu SC, Wang XY, Meng ZR, Deng QC, Peng EF, Yu CC, Hu X, Zhao Y, Ke YC, Qi FZ (2019) The mechanical properties, microstructures and mechanism of carbon nanotube-reinforced oil well cement-based nanocomposites. RSC Adv 9. https://doi.org/10.1039/C9RA04723A

5. Prusty K, Patra S, Swain SK (2020) Nano zno imprinted dextran hybrid poly (n-isopropylacrylamide)/poly ethylene glycol composite hydrogels for in vitro release of ciprofloxacin – sciencedirect. https://doi.org/10.1016/j.mtcomm.2020.101869

6. Zhang L, Du G, Zhou B, Wang L (2014) Green synthesis of flower-like zno decorated reduced graphene oxide composites. Ceram Int 40(1):1241–1244. https://doi.org/10.1016/j.ceramint.2013.06.023

7. Zhou L, Ju Y, Liao F, Yang Y, Wang X (2016) Improve the mechanical property and flame retardant efficiency of the composites of poly(lactic acid) and resorcinol di(phenyl phosphate) (rdp) with zno-coated kenaf. Fire Mater 40(1):129–140. https://doi.org/10.1002/fam.2274

8. Liang JZ (2009) Mechanical properties of pps/pc/gf/nano-caco3hybrid composites. Polym-Plast Technol Eng. https://doi.org/10.1080/03602550802675629

9. Kuang J, Zhang C, Meng Y (2015) Hyperbranched polyphenylene sulfide as stabilizer to prepare colloidal silver nanoparticles. Asian J Chem 27(11):4034–4036. https://doi.org/10.14233/ajchem.2015.19067

10. Najim AS, Ola AK (2016) Enhancement of tribological and mechanical behavior of polyphenylene sulfide reinforced by

titanium dioxide nanoparticles. Key Eng Mater 724:20–27. https://doi.org/10.4028/www.scientific.net/KEM.724.20

11. Wang X, Lu X, Bo X, Liu J (2013) Preparation and characteristic research on composites of polyphenylene sulfide modified by nano-silicon dioxide. Int Bhurban Confe Appl Sci Technol IEEE. https://doi.org/10.1109/IBCAST.2013.6512123

12. Yang J, Tao X, Ai L, Qin Z, Hong T, Qiang F (2009) Preparation and properties of poly (p-phenylene sulfide)/multiwall carbon nanotube composites obtained by melt compounding. Compos Sci Technol 69(2):147–153. https://doi.org/10.1016/j.compscitech.2008.08.030

13. Zhang M, Wang X, Bai Y, Li Z, Cheng B (2017) C60 as fine fillers to improve poly(phenylene sulfide) electrical conductivity and mechanical property. Rep 7(1):4443. https://doi.org/10.1038/s41598-017-04491-1

14. Sui M, Zhang L, Sheng L, Huang S, She L (2013) Synthesis of ZnO coated multi-walled carbon nanotubes and their antibacterial activities. Sci Total Environ 452–453:148–154. https://doi.org/10.1016/j.scitotenv.2013.02.056

15. Heerden J, Swanepoel R (1997) Xrd analysis of zno thin films prepared by spray pyrolysis. Thin Solid Films 299(1–2):72–77. https://doi.org/10.1016/S0040-6090(96)09281-4

16. Caramaro L, Chabert B, Chauchard J et al (1991) Morphology and mechanical performance of polyphenylenesulfide carbon fiber composite. Polym Eng Sci 31(17):1279–1285. https://doi.org/10.1002/pen.760311708

17. Riccò T, Pavan A, Danusso F (2004) Micromechanical analysis of a model for particulate composite materials with composite particles-survey of craze initiation. Polym Eng Sci 18(10):774–780. https://doi.org/10.1002/pen.760181007

18. Galán-Vidal CA, MuOz J, Dom Nguez C, Alegret S (1998) Glucose biosensor strip in a three electrode configuration based on composite and biocomposite materials applied by planar thick film technology. Sens Actuators B Chem 52(3):257–263. https://doi.org/10.1016/S0925-4005(98)00276-7

19. Chukov DI, Stepashkin AA, Tcherdyntsev VV, Olifirov LK, Kaloshkin SD (2017) Structure and properties of composites based on polyphenylene sulfide reinforced with al-cu-fe quasicrystalline particles. J Thermoplast Compos Mater 089270571772901. https://doi.org/10.1177/0892705717729015

20. Patterson SJ (1975) A lattice-point problem in hyperbolic space. Mathematika. https://doi.org/10.1112/S0025579300008834

21. Jog JP, Bulakh N, Nadkarni VM (1994) Crystallization of polyphenylene sulfide. Bull Mater Sci 17(6):1079–1089. https://doi.org/10.1007/BF02757585

22. Pamphilis NA (1989) Compositional analysis of polyphenylene sulfide containing ptfe and carbon fibers. Thermochim Acta 142(1):151–164. https://doi.org/10.1016/0040-6031(89)85015-4

23. Arici A (2005) Influence of annealing on the performance of short glass fiber-reinforced polyphenylene sulfide (pps) composites. J Compos Mater 39(1):21–33. https://doi.org/10.1177/0021998305046432

24. Diez-Pascual AM, Naffakh M (2012) Synthesis and characterization of nitrated and aminated poly(phenylene sulfide) derivatives for advanced applications. Mater Chem Phys 131(3):605–614

25. Kissinger HE (1957) Reaction kinetics in differential thermal analysis. Anal Chem 29(11):1702–1706

26. Zuo P, Tcharkhtchi A, Shirinbayan M, Fitoussi J, Bakir F (2020) Effect of thermal aging on crystallization behaviors and dynamic mechanical properties of glass fiber reinforced polyphenylene sulfide (PPS/GF) composites. J Polym Res 27(3):1–11

27. Betke U, Mcmullen P (1985) Lattice points in lattice polytopes. Mon Hefte Math 99(4):253–265. https://doi.org/10.1007/BF01312545

28. Levin AA, Syrkin YK, Dyatkina ME (1966) The chemical bond in crystals with an antifluorite structure and the valence possibilities of negative ions. J Struct Chem 7(6):806–809. https://doi.org/10.1007/bf00761156

29. Shang SW, Williams JW, Derholm KS (1992) Using the bond energy density to predict the reinforcing ability of a composite. J Mater Sci 27(18):4949–4956. https://doi.org/10.1007/BF01105259

30. Yang H, Ren S, Li Y, Li Z (2007) Preparation and antimicrobial property of organic-inorganic composite antimicrobial agents. Bull Chin Ceram Soc 1(2):223–226. https://doi.org/10.1166/jcp.2009.1042

31. Ol'Khov AA, Iordanskii AL, Zaikov GE, Shibryaeva LS, Litvinov IA, Vlasov SV (2000) Morphologically special features of poly(3-hydroxybutyrate)/low-density polyethylene blends. Polym-Plast Technol Eng. https://doi.org/10.1081/ppt-100101403

32. Ali N, Shadi R (2011) The effects of zno2 nanoparticles on strength assessments and water permeability of concrete in different curing media. Mater Res 14(2):178–188. https://doi.org/10.1590/s1516-14392011005000030

33. Ren W, Yang Y, Yang J, Duan H, Zhao G, Liu Y (2021) Multi-functional and corrosion resistant poly(phenylene sulfide)/ag composites for electromagnetic interference shielding. Chem Eng J. https://doi.org/10.1016/j.cej.2021.129052

34. Tsou CH, Wu CS, Hung WS, De Guzman MR, Gao C, Wang RY et al (2019) Rendering polypropylene biocomposites antibacterial through modification with oyster shell powder - sciencedirect. Polymer 160:265–271. https://doi.org/10.1016/j.polymer.2018.11.048

35. Wen YH, De Guzman MR et al (2020) NANO Brief Rep Rev 15(9):2050112 .https://doi.org/10.1142/S179329202050112X

36. Yao YL, De Guzman MR, Duan C et al (2020) Infusing high-density polyethylene with graphene-zinc oxide to produce antibacterial nanocomposites with improved properties. Chin J Polym Sci 38(08):155–166. https://doi.org/10.1007/s10118-020-2392-z

37. Ge FF, Tsou CH et al (2021) Barrier performance and biodegradability of antibacterial poly(butylene adipate-co-terephthalate) nanocomposites reinforced with a new MWCNT-ZnO nanomaterial. Nanotechnology 32:485706

38. Jiang S, Zhang Z, Hua Y et al (2011) Effects of hydroxyl and carboxyl modified multi walled carbon nanotubes on the crystallization properties of polyphenylene sulfide. Polym Mater Sci Eng 27(8):3. CNKI:SUN:GFZC.0.2011–08–021

39. Naeimi A, Khoshkam S, Eslaminejad T et al (2021) Natural cellulose fibers from Quinoa wastes reinforced carbon nanotube/ZnO bio-nanocomposite as a novel recyclable catalyst for oxidation reaction. Polym Bull 1–14

40. Luo Z, Zhang Z, Wang W et al (2009) Effect of polytetrafluoroethylene gradient-distribution on the hydrophobic and tribological properties of polyphenylene sulfide composite coating. Surf Coat Technol 203(10):1516–1522

41. Warner JW, Stephen Berry R (1985) Berry Hund's rule. Nature 313(160). https://doi.org/10.1038/313160a0

42. Guo J, Tsou CH, Yu Y et al (2021) Conductivity and mechanical properties of carbon black-reinforced poly(lactic acid) (PLA/CB) composites. Iran Polym J 30:1251–1262

43. Yao YL, De Guzman MR, Duan H et al (2020) Infusing High-density Polyethylene with Graphene-Zinc Oxide to Produce Antibacterial Nanocomposites with Improved Properties. Chin J Polym Sci 38:898–907. https://doi.org/10.1007/s10118-020-2392-z

44. Ma ZL, Tsou CH, Yao YL, De Guzman MR et al (2021) Ind Eng Chem Res 60(35):12911–12922. https://doi.org/10.1021/acs.iecr.1c02143

45. Chen ZJ, Tsou CH, Tsai ML et al (2021) Barrier properties and hydrophobicity of biodegradable poly(lactic acid) composites reinforced with recycled Chinese spirits distiller's grains. Polymers 13:2861. https://doi.org/10.3390/polym13172861

Authors and Affiliations

Fei-Fan Ge[1,2] · **Neng Wan**[1,2] · **Chi-Hui Tsou**[1,2,3] ⃝ · **Jui-Chin Chen**[4] · **Chin-San Wu**[5] · **Manuel Reyes De Guzman**[1,2,3] · **Chun-Yan Zeng**[1,2] · **Li Zhou**[1,2] · **Yu-Ting Wang**[1,2] · **Xu Luo**[1] · **Yong-Qi Yu**[1,2]

[1] School of Materials Science and Engineering, Sichuan University of Science & Engineering, Zigong 643000, China

[2] Material Corrosion and Protection Key Laboratory of Sichuan Province, School of Materials Science and Engineering, Sichuan University of Science & Engineering, Zigong 643000, China

[3] Sichuan Zhixiangyi Technology Co, Ltd, Chengdu 610051, People's Republic of China

[4] Department of Materials and Textiles, Oriental Institute of Technology, Pan, Chiao 22064, Taiwan

[5] Department of Applied Cosmetology, Kao Yuan University, Kaohsiung County 82101, Taiwan